



Three-dimensional modeling of polarization characteristics in molten carbonate fuel cells using peroxide and superoxide mechanisms

M.Y. Ramandi ^{a,*}, P. Berg ^b, I. Dincer ^a

^a Faculty of Engineering and Applied Science, University of Ontario Institute of Technology, Oshawa, Canada L1H 7K4

^b Faculty of Science, University of Ontario Institute of Technology, Oshawa, Canada L1H 7K4

HIGHLIGHTS

- A detailed three-dimensional, mathematical model of an MCFC was presented.
- Both peroxide and superoxide mechanisms predicted the linear region of the polarization curve accurately.
- Both mechanisms showed a concave tendency for the cathode reaction rate as the carbon-dioxide mole fraction is decreased when the current density increases.
- None of these mechanisms showed a downward bent in the polarization curve.

ARTICLE INFO

Article history:

Received 1 March 2012

Received in revised form

14 June 2012

Accepted 16 June 2012

Available online 3 July 2012

Keywords:

Molten carbonate fuel cell

Cathode reaction mechanism

Polarization characteristics

Voltage losses

Computational fluid dynamics

ABSTRACT

Polarization curves for the porous lithiated NiO cathode are very often reported with a linear slope over a wide potential range. However, the MCFC behaviour at higher oxidant utilization, when the mass transfer becomes dominant, is mostly overlooked. Therefore, in this study, the two most common cathode mechanisms are utilized to compare their prediction capabilities at higher current densities. This is performed by means of a three-dimensional, non-isothermal mathematical model which is developed by employing volume-averaged equations. As an extension to previous studies, the presented model also considers the potential and current density variation in both solid electrode and liquid electrolyte phases. In essence, this model is a set of partial differential equations including conservation of mass, momentum, gaseous species, energy, electronic potential and ionic potential that are solved using a finite volume method. In brief, both peroxide and superoxide mechanisms predict the linear region of the polarization curve accurately. However, none of these mechanisms showed a downward bent in the polarization curve. A positive exponent for the oxygen mole fraction is essential in obtaining the downward bent knee at high current densities which is in contrast to what has been reported in the literature to-date.

© 2012 Elsevier B.V. All rights reserved.

1. Introduction

Molten carbonate fuel cells (MCFCs) are deemed to be one of the most promising energy conversion devices that generate electricity and heat directly from oxidation of a gaseous or gasified fuel. Due to the high efficiency, high temperature, quiet operation, flexibility on fuel and, most importantly, zero emissions, MCFCs have become an attractive emerging technology for stationary co-generation of heat and power. Many efforts have been made in the past few decades to facilitate the commercialization of molten carbonate fuel cells and some of the technological concerns are addressed in [1].

Nonetheless, higher efficiencies and sufficiently elongated operating lifetimes with the least performance degradation have received much attention in research [1,2].

Generally, adequate models of porous electrodes would aim to enable researchers to illustrate precisely the relation between the MCFC performance and the structure of pores. This has been a major subject of debate among researchers and several models have been developed to simulate the behaviour of porous gas-diffusion electrodes. Furthermore, it is realized that polarization curves for the porous lithiated NiO cathode are very often reported with a linear slope over a wide potential range while unit cell behaviour at higher oxidant utilization, when the mass transfer becomes dominant, is mostly overlooked. Therefore, the goal of this paper is to develop a three-dimensional mathematical model and investigate polarization characteristics at higher oxidant

* Corresponding author. Tel.: +1 6479695880; fax: +1 9057213370.

E-mail addresses: Masoud.Youseframandi@uoit.ca (M.Y. Ramandi), Peter.Berg@uoit.ca (P. Berg), Ibrahim.Dincer@uoit.ca (I. Dincer).

Nomenclature

A_v	electrode active surface area ($\text{m}^2 \text{m}^{-3}$)	$\lambda_1, \lambda_2, \lambda_3$	anode reaction order
A	electrode–electrolyte interface area (m^2)	γ_1, γ_2	anode reaction order
c_p	specific heat ($\text{J kg}^{-1} \text{K}^{-1}$)	τ	tortuosity
D	mass diffusivity ($\text{m}^2 \text{s}^{-1}$)	ϵ	porosity
D_p	pore diameter (m)	θ	electrolyte filling degree
E_{eq}	equilibrium electric potential (V)	η	overpotential (V)
E_k	apparent activation energy in Eq. (35) (K^{-1})	μ	dynamic viscosity ($\text{kg m}^{-1} \text{s}^{-1}$)
F	Faraday's constant, 96,485 (C mol^{-1})	ν	species stoichiometric coefficient of the reaction
i_0	exchange current density (A m^{-2})	ρ	density (kg m^{-3})
i_0^0	reference exchange current density (A m^{-2})	φ	electric potential (V)
J	local current density (A m^{-2})	σ	electric conductivity of the solid phase (S m^{-1})
\bar{J}	average current density (A m^{-2})	κ	electric conductivity of the electrolyte phase (S m^{-1})
R	volumetric current density (A m^{-3})	k_0	pre-exponential factor in Eq. (35) (S m^{-1})
k	thermal conductivity ($\text{W m}^{-1} \text{K}^{-1}$)		
K	permeability (m^2)		
M	molecular weight (g mol^{-1})		
n	number of electrons		
P	static pressure (Pa)		
p_1, p_2, p_3	concentration exponents in anode reaction		
q_1, q_2, q_3	concentration exponents in cathode reaction		
R	universal gas constant ($8.314 \text{ J mol}^{-1} \text{ K}^{-1}$)		
S	molar entropy ($\text{J mol}^{-1} \text{ K}^{-1}$)		
S	source terms		
t	time (s)		
T	temperature (K)		
\vec{v}	gas velocity (m s^{-1})		
X	molar fraction		
Y	mass fraction		
<i>Greek letters</i>			
α	transfer coefficient		
<i>Subscripts and superscripts</i>			
a	anode		
agc	anode gas channel		
c	cathode		
cgc	cathode gas channel		
e	electrolyte phase		
g	gas phase		
in	inlet		
i	i th component		
j	j th species		
m	mass equation		
out	outlet		
s	solid phase		
T	Energy equation		
u	momentum equation		
φ_e	electronic charge equation		
φ_c	carbonate ion charge equation		
eff	effective		
ref	reference state		

utilization. Furthermore, it is desired to compare the prediction capabilities of the two most common cathode reaction mechanisms, namely the peroxide and superoxide mechanisms.

The simplest electrode model, the so-called Simple (or Flooded) Pore Model, was introduced by Austin et al. [3] in 1965. The problem associated with this primitive model was the very poor performance prediction due to severe mass transfer limitation. Since then researchers have tried to introduce corrections to this model which led to the Thin Film Model [4,5] and the Finite-Contact-Angle Meniscus Model [6] which are extensions of the simple pore model and account for variations in the wetting tendency of the electrolyte. In a flooded pore with finite-angle meniscus the current is predominantly concentrated in a small portion of the pore wall. Whereas in a film-covered pore, the electrochemical reaction still has a propensity to be concentrated in the part of the film which is closest to the bulk electrolyte. Later on, the migration of reactants on the surface of the electrode was incorporated by Iczkowski [7].

Bearing in mind all these cited studies a more realistic porous electrode model ought to consider a spectrum of pore sizes. For that reason, several dual-porosity models were introduced [8–10]. The Standard Agglomerate Model, presented by Giner and Hunter [11], presumes an idealized electrode in which the pores are divided into two forms. The micro-pores are assumed to be completely flooded with electrolyte, while the macro-pores are thought to enclose only gas. The model has been reasonably successful in predicting the performance of fuel cells. The agglomerate model characterizes electrode structure more satisfactorily than the thin film model [12]. However, the anode and cathode have different wetting

characteristics. Wilemski [13] proposed individual porous electrode models for the anode and cathode of a molten carbonate fuel cell. In this model all electrochemical activity is assumed to take place on film-covered walls of the larger gas filled pores. Smaller flooded pores were treated as electrochemically inert. The model showed good agreement with experimental data. Nevertheless, it oversimplifies pore structure, and requires measured values for film areas and thicknesses, forcing these parameters to be treated empirically. Afterwards, Kunz et al. [14] modified the conventional agglomerate model and developed a homogeneous model by calculating the effective agglomerate diameter, porosity and tortuosity based on the electrode's pore spectrum and electrolyte content. Many researchers have used this theory and developed it further. Jewulski and Suski [15] proposed an isotropic steady state, one-dimensional model for the porous anode of an MCFC which required the thickness of the electrolyte film in the pores as the only adjustable parameter. Later on Jewulski [16] applied this model for the porous cathode as well. Yuh and Selman [12] developed a steady state, two-dimensional dual-porosity agglomerate-type model for the porous electrodes. The proposed model involves a more complicated expression instead of the Ohm's law to include ionic migration in the melt. They employed this model to predict the electrode performance. Lee et al. [17] indicated that the resulting values of the fit parameters depend strongly on the choice of the agglomerate radius (or slab width), the film thickness, and the electrolyte conductivity. These radii and film thicknesses are very difficult to determine meaningfully. Furthermore, because of its geometric restrictions, it is difficult to incorporate the electrolyte filling degree into the agglomerate model.

Another problem of the agglomerate model is that the model does not accurately predict the optimal degree of filling [18].

However, all the previous stated models are based on a continuum approach to modeling. Prins-Jansen et al. [19] chose to use a more fundamental approach named Agglomerate-Like Model which is based on averaging of equations that describe the processes on the micro-scale. This model eliminates the important drawback of the preceding agglomerate model caused by geometric assumptions and restrictions. Unlike the agglomerate model, the new model is suitable for studying three-dimensional and anisotropic problems, and incorporates the degree of electrolyte filling. Fontes et al. [20] used a steady state two-dimensional pseudo-homogeneous model for the three-phase system of the cathode and involved the polarization curves from the heterogeneous agglomerate model as local source function. They showed that the geometry of the gas holes in the current collector can influence the performance of the electrode due to the non-uniform lateral distribution of the current production. They [21] also used the homogeneous and heterogeneous agglomerate model for one and two-dimensional calculations, respectively, to explain the influence of gas phase mass transfer on the performance of the porous MCFC cathodes. The results showed that for standard gas composition and normal operating current density, the effect of gas-phase diffusion is small. In addition, for low oxygen partial pressures, the influence of mass transfer limitations appears to be large even at low current densities, which makes kinetic studies very difficult. In a newer model, called Electrochemical-Potential Model [22], the electrochemical potentials for individual species are combined to define component potentials which are separated by the slow chemical and/or electrochemical reactions. Then, the reaction rates for the slow reactions are assumed to be proportional to the differences in these component potentials. Fehribach et al. [23] employed this model for the peroxide mechanism describing the electrochemistry of an MCFC cathode. Fehribach and Hemmes [24] compared the polarization losses associated with the various diffusion-reaction-conduction processes in MCFC cathodes. They estimated each type of polarization loss in terms of component electrochemical potentials. The main advantage of the component-potential approach is that it simplifies both the analysis and the computations. Also, Subramanian et al. [25,26] employed the three-phase homogeneous model of Prins-Jansen et al. [19] and reported the performance analysis results based on a one-dimensional model.

Despite all of these remarkable efforts in developing porous electrode mathematical models, temperature variation effects are still overlooked. Moreover, hydrodynamics of gas flow in the gas channels are disregarded. As well, the effect of convective mass flux is passed over. More to the point, three-dimensional studies based on a volume-averaging technique seems to be absent in the literature. Last but not the least, unit cell behaviour at extreme gas utilization is rarely reported.

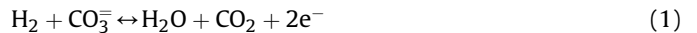
As a consequence, the foremost intention of this study is to present a three-dimensional, non-isothermal model by employing the volume-averaged equations used by Prins-Jansen et al. [27]. As a modification, instead of using a single equation for electric potential, electronic and ionic potential equations are introduced and solved separately. Hence, the presented model considers the potential and current density variation in both solid electrode and liquid electrolyte phases. As another contribution, gas channels are considered explicitly in our mathematical modeling and convection-diffusion mechanisms are taken into account. Another modification is performed by considering the degree of electrolyte filling of unit cell components.

Fundamentally, this model is a set of partial differential equations including conservation of mass, momentum, gaseous species, energy, electronic potential and ionic potential. This mathematical

model will be implemented for our future transient, three-dimensional unit cell and stack level simulations. However, in this research the model is utilized to offer an improved insight into the polarization characteristics of molten carbonate fuel cells. To accomplish this, the equations are discretized and solved with ANSYS FLUENT [28], a finite volume-based commercial software. Meanwhile, the programming language C is utilized to develop a complementary module in which the MCFC model details are integrated. The developed mathematical model is then used to predict unit cell behaviour at high cathode gas utilizations.

2. Problem formulation

Fig. 1 schematically demonstrates the three-dimensional physical domain of an MCFC divided into five sub-domains: the anode gas channel (AGC), anode, electrolyte, cathode and cathode gas channel (CGC). The fuel gas which is a gaseous mixture of hydrogen, water vapour and carbon-dioxide enters the AGC and diffuses through the porous anode where hydrogen molecules are subjected to the hydrogen oxidation reaction (HOR). During this electrochemical reaction, hydrogen combines with carbonate ions, ending with water vapour and carbon-dioxide as follows:



The released electrons migrate through an external circuit, create electricity and return to the cell through the cathode. On the cathode side, a mixture of oxygen, carbon-dioxide and nitrogen enters the cathode gas channel and diffuses through the porous cathode, where the oxygen reduction reaction (ORR) takes place. Oxygen is reduced to carbonate ions by combining with carbon-dioxide and the electrons coming from the external circuit as



The carbonate ions formed at the cathode move through the electrolyte toward the anode, carrying the electric current and completing the carbon-dioxide circuit. The structural parameters of the simulated MCFC are summarized in Table 1.

A comprehensive MCFC model needs to consider the transport of the multi-component gas species in gaseous and liquid phases, electrochemical and chemical reaction kinetics, heat generation, heat transfer, transport of the electrons and carbonate ions, and porous electrode effects. These processes occur in void volumes, liquid phase, solid phase and at triple-phase boundaries (TPB).

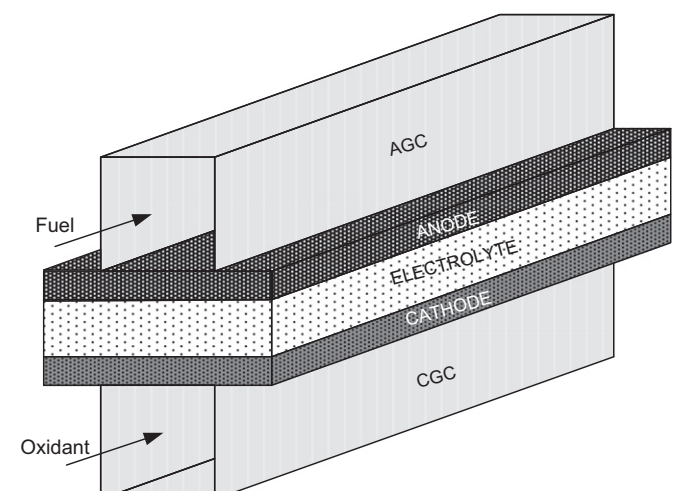


Fig. 1. The physical domain of the simulated MCFC.

Table 1

The structural parameters of the simulated MCFC.

Parameter	Value
Cell length, mm	100
Anode gas channel height, mm	2.0
Anode gas channel width, mm	2.0
Cathode gas channel height, mm	2.0
Cathode gas channel width, mm	2.0
Anode height, mm	0.7
Anode width, mm	4.0
Cathode height, mm	0.6
Cathode width, mm	4.0
Electrolyte height, mm	1.0
Porosity of anode, ϵ_a [31]	0.52
Porosity of cathode, ϵ_c [31]	0.62

Without losing the generic physical characteristics, every numerical simulation is conceived and developed based on a set of assumptions motivated by a lack of experimentally evaluated physical parameters. Likewise, the following assumptions are made for this model: (i) the chemical species obey the ideal gas law and are ideally mixed; (ii) the porous anode and cathode are homogeneous; (iii) the effects of gravity are negligible; (iv) the anodic and cathodic electrochemical reactions take place at the three-phase boundaries inside the electrodes; (v) in anode and cathode sub-domain, the gas mixture and solid component are in a thermal equilibrium state (have identical temperature) and hence one equation with effective heat conductivity can describe the heat transport process; (vi) both anodic and cathodic electrochemical reactions follow the Butler–Volmer equation; (vii) any change in the concentration of carbonate ions inside the electrolyte is negligible.

2.1. Governing equations

This section exhibits the general form of governing equations implemented to model the MCFC. In contrast to the approach that employs separate differential equations for different sub-domains, in this study, the ‘single-domain approach’ is utilized. This approach considers a single set of governing equations for all sub-domains. However, for each sub-domain model input parameters (diffusivities, conductivities, etc.) are specified separately. As a result, no interfacial conditions are required to be specified at internal boundaries between various sub-domains. Prior to describing each specific governing equation, it is worthwhile to point out that each phenomenon can be described with a separate partial differential equation which comprises a transient term, diffusion term, convection term and a source term. By taking all these terms into account, a general equation can be derived in the form

$$\frac{\partial}{\partial t}(\rho\Theta) + \nabla \cdot (\rho \vec{u}\Theta - \Gamma_\Theta \nabla \Theta) = S_\Theta \quad (3)$$

where Θ is 1, u , Y , h , ϕ_{ele} and ϕ_{ion} in the continuity, momentum, species, energy, electronic and ionic potential equations, respectively. Γ_Θ and S_Θ are the diffusion coefficient and source terms which have consistent units.

An appropriate approach is needed to model the porous electrodes. In general, the agglomerate model divides the porous media into a number of micro-pores and macro-pores, followed by averaging the two-phase equations over the micro-porous regions which makes it difficult to justify the model rigorously. Essentially, in this approach a few assumptions concerning pore structure (agglomerate radius and electrolyte film thickness) are unavoidable. Hence, in this study a more realistic approach commonly used in porous media problems, the so-called volume averaging, is employed. However, according to porous-media theory, it must be feasible to define representative control volumes (unit cells) for the

volume-averaging process to be meaningful. The size of a unit cell must be chosen with the intention that a change in the size and/or position of the cell has an insignificant effect on the porosity of the cell. This implies that it must be considerably larger than the length scale of micro-porosity, but much smaller than the scale on which significant changes in macroscopic quantities arise. In this model, all three phases are taken into account. By doing so, a large enough unit cell can be defined, and this makes it possible for a unit cell to fulfill the requirements for averaging. In contrast to the agglomerate model, the new model is suitable for studying three-dimensional and anisotropic problems, and integrating the degree of electrolyte filling. In actual fact, this model is based on the basic mass and current balances at the micro-scale which, subsequently, are averaged (homogenized) across all three phases (solid/gas/liquid) of the electrode to yield the macro-scale level equations. In the following sections, the macro-scale governing equations are illustrated. Readers are referred to Prins-Jansen et al. [27] for more details on the averaging technique.

■ Conservation of mass

To begin with, the transport of any gas species has to satisfy the conservation of mass and momentum. The total mass gain in the anode is equal to the mass loss in the cathode. This can be justified by considering the production and consumption of carbon-dioxide. Clearly, for each mole of CO_2 produced in the fuel flow, a mole of CO_2 is consumed in the oxidant flow due to conservation of electric charges (Eqs. (1) and (2)). Therefore, the conservation of mass is written as [29]:

$$\frac{\partial}{\partial t}(\epsilon^{\text{eff}} \rho_g) + \nabla \cdot (\rho_g \vec{u}_g) = S_m \quad (4)$$

where ρ_g and \vec{u}_g are the superficial values of the gas mixture density and velocity, respectively. S_m ($\text{kg m}^{-3} \text{s}^{-1}$) is the mass source term which has different values depending on the cell sub-domain. The gas mixture density (kg m^{-3}) is calculated based on the ideal gas law [29]:

$$\rho_g = P_g \left(RT \sum_i \frac{Y_i}{M_i} \right)^{-1} \quad (5)$$

where P_g is the superficial value of the gas pressure (Pa), T the temperature (K), R the universal gas constant ($\text{J kmol}^{-1} \text{K}^{-1}$). In addition, Y_i and M_i are mass fraction and molecular weight (kg kmol^{-1}) of species i , respectively.

It is crucial to indicate that the actual volume fractions of the gas in porous anode and cathode are less than the electrode porosity (ϵ). This is a result of the volume percentage occupied by the electrolyte, namely the electrolyte filling degree (θ), which is present in liquid form. Hence, an effective porosity (ϵ^{eff}) is defined and implemented in the governing equation as well as in constitutive laws

$$\epsilon^{\text{eff}} = \epsilon(1 - \theta) \quad (6)$$

■ Conservation of momentum

The general form of the conservation of momentum equation can be written as [29]:

$$\frac{\partial}{\partial t} \left(\frac{1}{\epsilon^{\text{eff}}} \rho_g \vec{u}_g \right) + \nabla \cdot \left(\frac{1}{(\epsilon^{\text{eff}})^2} \rho_g \vec{u}_g \vec{u}_g \right) = -\nabla P_g + \nabla \cdot (\bar{\tau}) + S_u \quad (7)$$

where S_u is the momentum volumetric sink term (Pa m^{-3}) which is zero in gas channels. It is determined in the porous electrodes using Darcy's equation [29]. This momentum sink contributes to the pressure gradient in the porous electrodes, creating a pressure drop that is proportional to the fluid velocity. For homogeneous porous media:

$$S_u = -\frac{\mu_g}{K_{\text{eff}}} \vec{u}_g \quad (8)$$

In this equation μ_g is the dynamic viscosity of the ideal gas mixture ($\text{kg m}^{-1} \text{s}^{-1}$) and it is calculated based on kinetic theory [29] as

$$\mu_g = \sum_i \frac{X_i \mu_i}{\sum_j X_i \psi_{ij}} \quad (9)$$

$$\psi_{ij} = \frac{\left[1 + \left(\mu_i/\mu_j\right)^{0.5} (M_i/M_j)^{0.25}\right]^{0.5}}{\left[8(1 + M_i/M_j)\right]^{0.5}} \quad (10)$$

where i and j represent different species. X_i is the mole fraction of species i . Furthermore, K_{eff} is the effective permeability of the porous media which depends on the relative permeability, K_r , and the intrinsic permeability, K_i , through the following equation [30]:

$$K_{\text{eff}} = K_r K_i \quad (11)$$

The relative permeability is determined by [30]:

$$K_r = (1 - \theta)^\gamma \quad (12)$$

Here, different values are used for the exponent. The widely used cubic correlation is empirical and comes from sand/rock-type porous media with a typical porosity of 0.1–0.4. Nonetheless, it is suggested to be between 4.0 and 5.0 for porous materials with porosities over 0.6 [30]. For MCFCs, it is recommended to be 1 [31]. Perceptibly, a combination of Eqs. (11) and (12) depicts that if the local pore volume of the anode or cathode is fully saturated with liquid electrolyte, the gas permeability will become zero, resulting in an infinite (negative) value for the momentum source term. The intrinsic permeability is an intensive property. It is a measure of the ability of the porous material to allow fluids to pass through it and is a function of the material structure only (and not of the fluid), and explicitly distinguishes the value from that of relative permeability. It is hard to find values for permeability in the literature for MCFCs. Findlay [32] utilized the values for the permeability in a proton exchange membrane fuel cell (PEMFC) which is $1.9 \text{ e}^{-12} \text{ m}^2$. On the other hand, the Carman–Kozeny relation for an aggregated bed of spheres [33,34] can be used to estimate the value of the permeability:

$$K = \frac{D_p^2}{150} \frac{\left(\epsilon^{\text{eff}}\right)^3}{\left(1 - \epsilon^{\text{eff}}\right)^3} \quad (13)$$

where D_p is the pore diameter of the porous material which is normally between 8 and 12 μm for MCFC electrodes [32,33]. By substituting this value in Eq. (13) and calculating the permeability, the value used by Findlay [32] can be justified. Also, in a CFD model developed by Jiao [35], the pore diameter of the catalyst layer is reported to be 24 μm and the permeability is estimated to be $6.2 \text{ e}^{-12} \text{ m}^2$. This obviously shows that $1.9 \text{ e}^{-12} \text{ m}^2$ is applicable for MCFCs which is also reported by Promislow et al. [36].

■ Conservation of gaseous species

To describe the chemical species transport, the general form of the conservation equation including both convection and diffusion terms, is considered:

$$\frac{\partial}{\partial t} \left(\epsilon^{\text{eff}} \rho_g Y_i \right) + \nabla \cdot \left(-\rho_g D_{i,\text{m}}^{\text{eff}} \nabla Y_i \right) + \nabla \cdot \left(\rho_g \vec{u}_g Y_i \right) = S_i \quad (14)$$

where i represents H_2 , H_2O and CO_2 in anode and O_2 , CO_2 and N_2 in cathode. Therefore, there are mainly five species to be considered in this study. In order to facilitate the solution procedure only the first four of the five species can be numerically resolved, leaving the fifth one to be determined through the following equation:

$$\sum_i Y_i = 1 \quad (15)$$

However, the mechanism of species transport in gas channels and porous electrodes are not identical. In gas channels, no electrochemical reaction exists and the multi-component gas species transport occurs. Therefore, in Eq. (14) the species mass source term, S_i , is zero. $D_{i,\text{m}}^{\text{eff}}$ is the effective mass diffusion coefficient of species i in the gas mixture and is determined by [29]:

$$D_{i,\text{m}}^{\text{eff}} = \frac{1 - X_i}{\sum_{i,j \neq i} \left(X_j / D_{ij}^{\text{eff}} \right)} \quad (16)$$

where D_{ij}^{eff} is the effective binary mass diffusion coefficient of species i in species j which is calculated by

$$D_{ij}^{\text{eff}} = D_{ij} \frac{T}{T^{\text{ref}}} \frac{P^{\text{ref}}}{P} \frac{\epsilon^{\text{eff}}}{\tau} \quad (17)$$

where D_{ij} is the bulk binary diffusivity at the reference temperature (T^{ref}) and reference pressure (P^{ref}). Also, τ is the tortuosity of the porous material which is frequently estimated by the following Bruggemann correlation in fuel cell modeling [30].

$$\tau = \left(\epsilon^{\text{eff}} \right)^{-0.5} \quad (18)$$

It is apparent that in gas channels the porosity is equal to one. The species transport mechanism of porous electrodes is a more complex scenario. Fig. 2 demonstrates a closer view of the porous electrode morphology. According to this figure, each volume-averaging cell encloses the solid electrode, gas mixture and liquid electrolyte. Mass transport occurs in the liquid and gas phases. Precisely, reactants diffuse through the gaseous mixture and then transfer to the molten electrolyte so as to reach the triple-phase boundary where the electrochemical reaction takes place. Hence, two equations can be written for species transport in gas and liquid

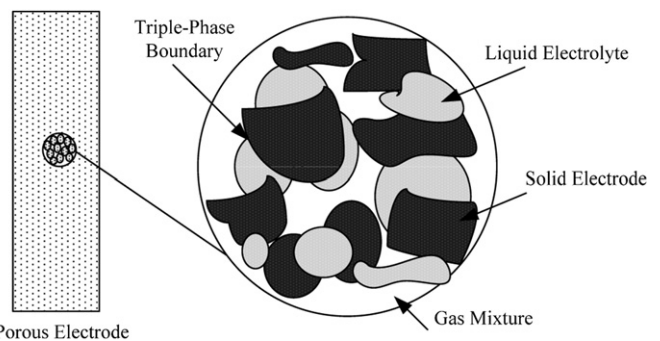


Fig. 2. Schematic of porous electrode (left) and volume-averaging cell enclosing the triple-phase boundaries (right).

phases at the micro-scale level, considering the fact that electrochemical reactions take place in the liquid phase only. Now, by defining a control volume resembling Fig. 2, the two phases (the gas and the electrolyte) could be effectively combined. Clearly, the physically observable quantities of interest (concentration) occur on a much larger macro-scale where micro-scale equations are not applicable. Rather, these micro-scale equations can be averaged using theorems from porous-media theory [37]. By doing so, it introduces average concentrations defined across both phases, represented by Eq. (14). Nevertheless, there is a major apprehension in regards to the diffusive flux terms which is related to the diffusion coefficients. It is said to be evaluated by a volume fraction-based average over the gas and liquid phase diffusivities [27]. In this study it is implemented as

$$D_{i,m}^{\text{eff}} = \left(\varepsilon(1-\theta) / \frac{1-X_i}{\sum_{i,j \neq i} (X_j/D_{ij}^g)} + \varepsilon\theta/D_i^l \right)^{-1} \quad (19)$$

where g and l corresponds to the gas and liquid phases respectively.

The source terms on the right hand side of Eqs. (4) and (14) are directly associated with the electrochemical reactions in anode and cathode. Over the past three decades, several studies have been carried out to find the anode and cathode reaction mechanisms that best represent the actual electrochemical reaction (e.g. [16]). The available proposed mechanisms are mostly based on the concept of rate-determining step.

The two most common reaction mechanisms for anode are proposed by Ang and Sammels [38] and Jewulski and Suski [15]. Boden et al. [31] incorporated both mechanisms in their mathematical modeling and achieved identical results. In this study, the former mechanism is employed

$$R_a = A_{v,a} \times i_{0,a} \left[\left(\frac{X_{H_2}}{X_{H_2,\text{in}}} \right)^{p_1} \exp\left(\frac{\alpha_{aa}F}{RT}\eta_a\right) - \left(\frac{X_{H_2}}{X_{H_2,\text{in}}} \right)^{p_2} \left(\frac{X_{H_2O}}{X_{H_2O,\text{in}}} \right)^{p_3} \left(\frac{X_{CO_2}}{X_{CO_2,\text{in}}} \right)^{p_4} \exp\left(-\frac{\alpha_{ca}F}{RT}\eta_a\right) \right] \quad (20)$$

In contrast, there are several reaction mechanisms that have been proposed for the cathode electrochemical reaction. In fact, the prediction capability of these mechanisms is rarely discussed in literature. Therefore, the two most common reaction mechanisms, namely the peroxide and superoxide mechanisms [12,14] are employed and compared in this paper. In any event, the general form of the cathode reaction equation reads

$$R_c = A_{v,c} \times i_{0,c} \left[\left(\frac{X_{CO_2}}{X_{CO_2,\text{in}}} \right)^{q_1} \left(\frac{X_{O_2}}{X_{O_2,\text{in}}} \right)^{q_2} \exp\left(\frac{\alpha_{ac}F}{RT}\eta_c\right) - \left(\frac{X_{CO_2}}{X_{CO_2,\text{in}}} \right)^{q_3} \left(\frac{X_{O_2}}{X_{O_2,\text{in}}} \right)^{q_4} \exp\left(-\frac{\alpha_{cc}F}{RT}\eta_c\right) \right] \quad (21)$$

where A_v , F and α are the electrode active surface area, Faraday constant and transfer coefficient, respectively. i_0 is the exchange current density [31], given by

$$i_{0,a} = i_{0,a}^0 (X_{H_2,\text{in}})^{\lambda_1} (X_{H_2O,\text{in}})^{\lambda_2} (X_{CO_2,\text{in}})^{\lambda_3} \quad (22)$$

$$i_{0,c} = i_{0,c}^0 (X_{O_2,\text{in}})^{\gamma_1} (X_{CO_2,\text{in}})^{\gamma_2} \quad (23)$$

where i_0^0 is the standard exchange current density and “in” donates inlet. The values of transfer coefficients and exponents for all

mechanisms are summarized in Table 2. The overpotential, η , is defined as

$$\eta_a = \phi_s - \phi_e \quad (24)$$

$$\eta_c = \phi_s - \phi_e - E_{\text{eq}} \quad (25)$$

here, ϕ_s and ϕ_e are solid phase and electrolyte phase potentials. Moreover, E_{eq} is the potential difference between solid and electrolyte phase potentials in equilibrium, i.e. when no current is generated, and is defined using the Nernst equation [39]:

$$E_{\text{eq}} = E_0 + \left[\frac{RT}{nF} \ln \left(\frac{P_{H_2,a} P_{CO_2,c} P_{O_2,c}^{0.5}}{P_{CO_2,a} P_{H_2O,a}} \right) \right] \quad (26)$$

$$E_0 = 1.2723 - 2.7645 \times 10^{-4} \text{ T} \quad (27)$$

Now, the production and consumption of various species involved in the anode and cathode reactions can be expressed as

$$S_{i,a} = \frac{\nu_{i,a} M_i R_a}{nF} \quad (28)$$

$$S_{i,c} = \frac{\nu_{i,c} M_i R_c}{nF} \quad (29)$$

where ν_i denotes the stoichiometric coefficient of species i . Also, the mass equation source term reads

$$S_m = \sum_i S_i \quad (30)$$

■ Conservation of electronic charge

The governing equation for the electronic charge transport in MCFCs can be derived by means of Ohm's law as follows:

$$\nabla \cdot (-\sigma^{\text{eff}} \nabla \phi_s) = S_{\phi_s} \quad (31)$$

where σ^{eff} is the effective electric conductivity of the solid material which is estimated based on the Bruggemann correlation. An exponent of 1.0 is used [31].

$$\sigma^{\text{eff}} = \sigma(1-\varepsilon)^{1.0} \quad (32)$$

Additionally, S_{ϕ_s} denotes the electron generation or consumption in the electrodes. It is determined by R_a in the anode and R_c in the cathode and is zero elsewhere.

■ Conservation of ionic charge

Similar to Eq. (31), the ionic charge is conserved through the following equation:

$$\nabla \cdot (\kappa^{\text{eff}} \nabla \phi_e) = S_{\phi_e} \quad (33)$$

Table 2
Reaction orders and species exponents in the electrochemical reaction rates.

Reaction mechanism	Reaction orders	Concentration exponents
Ang & Sammels (anode)	$\lambda_1 = 0.25, \lambda_2 = 0.25, \lambda_3 = 0.25$	$p_1 = 0.5, p_2 = -0.5, p_3 = 1, p_4 = 1$
Peroxide (cathode)	$\gamma_1 = 0.375, \gamma_2 = -1.25$	$q_1 = 0, q_2 = -2, q_3 = 0.5, q_4 = -1$
Superoxide (cathode)	$\gamma_1 = 0.625, \gamma_2 = -0.75$	$q_1 = 0, q_2 = -2, q_3 = 0.75, q_4 = -0.5$

where κ^{eff} is the effective electric conductivity in the liquid phase which is approximated based on the following correlation for electrodes [31]

$$\kappa^{\text{eff}} = \kappa(\epsilon\theta)^{1.5} \quad (34)$$

According to this study, the effective conductivity of the pore electrolyte in the anode is $0.03\text{--}93\text{ S m}^{-1}$, depending on the degree of electrolyte filling. However, the following correlation is used to estimate the ionic conductivity [40]

$$\kappa = \kappa_0 \exp(-E_k/T) \quad (35)$$

In addition, S_{ϕ_e} denotes the carbonate ion generation or consumption in the electrodes. It is determined by R_a in the anode and R_c in the cathode while it vanishes elsewhere.

■ Conservation of energy

It is assumed that the gas mixture and solid components of the fuel cell are in a thermal equilibrium state [41]. Thus, only one energy equation will be solved for each cell region. As such, the energy equation applying to each individual zone of the fuel cell can be written as [29]:

$$\frac{\partial}{\partial t} \left(\sum_{k=\text{g,s,e}} (\epsilon \rho c_p)_k T \right) + \nabla \cdot (-k^{\text{eff}} \nabla T) + \nabla \cdot (\vec{u}_g \epsilon \rho_g c_p T) = S_T \quad (36)$$

The first term on the left hand side accounts for all three phases available in each individual sub-domain which incorporates the volume-averaged values of material properties. k^{eff} is the effective thermal conductivity, determined by

$$k^{\text{eff}} = (1 - \epsilon)k_s + \epsilon(1 - \theta)k_g + \epsilon\theta k_e \quad (37)$$

where k_s , k_g and k_e are the thermal conductivity of solid material, gas mixture and liquid electrolyte, respectively. Similar to the dynamic viscosity, kinetic theory is used to determine the thermal conductivity of the gas mixture as follows:

$$k_g = \sum_i \frac{X_i k_i}{\sum_j X_j \psi_{ij}} \quad (38)$$

The heat generation or consumption is represented by the source term, S_T . Three kinds of heat sources in the electrodes are considered in the presented model, namely the reversible heat release during the electrochemical reaction, irreversible or activation heat generation and ohmic heating. The only heat source in the electrolyte is due to ohmic heating which is evaluated by

$$S_T = \frac{J_e^2}{\kappa} \quad (39)$$

In the anode, all three types of heat generation mechanisms are present. Hence, we have

$$S_T = \frac{J_e^2}{\kappa_a} + \frac{J_s^2}{\sigma_a} + |\eta_a R_a| + \left| \frac{R_a}{nF} \right| (T \Delta S_a) \quad (40)$$

Likewise, the source term in the cathode is

$$S_T = \frac{J_e^2}{\kappa_c} + \frac{J_s^2}{\sigma_c} + |\eta_c R_c| + \left| \frac{R_c}{nF} \right| (T \Delta S_c) \quad (41)$$

In the gas flow channels no heat generation occurs. In the above equations, J_s and J_e are the magnitude of electronic and ionic

current density, respectively. These parameters are related to the potentials through Ohm's law:

$$\vec{J}_s = -\sigma \nabla \phi_s \quad (42)$$

$$\vec{J}_e = \kappa \nabla \phi_e \quad (43)$$

One of the objectives of the present article, unlike previous studies, is to provide all required model input parameters to help the reader have a better understanding of the model. Hence, the electrochemical kinetic parameters are summarized in Table 3. As well, Table 4 exhibits all physical and thermal properties of the materials involved in the mathematical modeling.

2.2. Boundary conditions

Based on the presented complete set of governing equations, there are 12 unknowns which needed to be solved for

$$u, v, w, P, Y_{\text{H}_2}, Y_{\text{H}_2\text{O}}, Y_{\text{CO}_2}, Y_{\text{O}_2}, Y_{\text{N}_2}, T, \phi_e, \phi_s$$

With the intention of completing the fuel cell model formulation, stating various boundary conditions at different positions is indispensable. The boundary conditions, for a computational domain with a single pair of gas flow channels, are illustrated in Fig. 3. It was elucidated earlier that the boundary conditions are vital only at the external surfaces of the computational domain due to the employed single-domain formulation. These are no-flux conditions everywhere with the exception of electrode/channel interfaces.

At the anode gas channel inlet (I_{agc}) and cathode gas channel inlet (I_{cgc}), the total mass flux, temperature and gas species composition of the entering gas flow are specified. Moreover, the fluxes of electric and ionic charge are considered to be zero. Additionally, considering the very large aspect ratio of the gas channels, the flow is assumed to be fully developed at the anode gas channel outlet (O_{agc}) and cathode gas channel outlet (O_{cgc}). This means, none of the variables and respective fluxes vary in the normal direction. Likewise, the gas pressure is specified. A thermally insulated no slip boundary condition is applied to the anode and cathode gas channel walls including, W_{agc}^T , W_{cgc}^B . The fluxes of electric and ionic charge are set to zero. For all other walls of the gas channels, $W_{\text{a,agc}}^L$, $W_{\text{a,agc}}^R$, $W_{\text{c,cgc}}^L$, and $W_{\text{c,cgc}}^R$, the electronic potential is specified while the fluxes corresponding to the remaining variables are set to zero. For the no-flux boundaries, W^L and W^R , the zero-flux condition is assumed for all variables.

2.3. Numerical study

The computational domain is divided into a number of control volumes using ANSYS ICEM CFD 12.0.1. The Finite Volume based commercial software, ANSYS FLUENT 12.0.1, is employed to discretize and solve the set of governing equations. These equations are strictly coupled through the source terms resulting from the electrochemical reactions. A set of under-relaxation techniques is developed to handle the divergence difficulties. Furthermore, the C programming language is used to develop a supplementary code in

Table 3
Electrochemical kinetic parameters.

Parameter	Value
Standard exchange current density of anode, $i_{0,a}^0$ (A m^{-2}) [38]	20–220
Standard exchange current density of cathode, $i_{0,c}^0$ (A m^{-2}) [27]	0.3–7.0
Active surface area of anode, $A_{v,a}$ ($\text{m}^2 \text{ m}^{-3}$) [31]	2.7E5
Active surface area of cathode, $A_{v,c}$ ($\text{m}^2 \text{ m}^{-3}$) [31]	3.0E5

Table 4

Physical and thermal properties of various materials.

Parameter	Value
Thermal conductivity of anode, k_a ($\text{W m}^{-1} \text{K}^{-1}$) [42,43]	78
Thermal conductivity of cathode, k_c ($\text{W m}^{-1} \text{K}^{-1}$) [42,43]	0.9
Thermal conductivity of electrolyte, k_e ($\text{W m}^{-1} \text{K}^{-1}$) [43]	2.0
Specific heat of anode, $c_{p,a}$ ($\text{J kg}^{-1} \text{K}^{-1}$) [46]	444
Specific heat of cathode, $c_{p,c}$ ($\text{J kg}^{-1} \text{K}^{-1}$) [46]	44,352
Specific heat of electrolyte, $c_{p,e}$ ($\text{J kg}^{-1} \text{K}^{-1}$) [46]	4000
Density of anode, ρ_a (kg m^{-3}) [46]	8220
Density of cathode, ρ_c (kg m^{-3}) [46]	6794
Density of electrolyte, ρ_e (kg m^{-3}) [46]	1914
Electric conductivity of anode, σ_a (S m^{-1}) [20,44]	100
Electric conductivity of cathode, σ_c (S m^{-1}) [20,44]	100
Free electrolyte conductivity: pre-exponential factor, κ_0 (S m^{-1}) [13]	3637
Free electrolyte conductivity: apparent activation energy, E_k (K^{-1}) [13]	3016
Hydrogen diffusivity in carbon-dioxide, $D_{\text{H}_2-\text{CO}_2}$ ($\text{m}^2 \text{s}^{-1}$) [46,47]	5.5E-5
Hydrogen diffusivity in water vapour, $D_{\text{H}_2-\text{H}_2\text{O}}$ ($\text{m}^2 \text{s}^{-1}$) [46,47]	9.15E-5
Oxygen diffusivity in carbon-dioxide, $D_{\text{O}_2-\text{CO}_2}$ ($\text{m}^2 \text{s}^{-1}$) [46,47]	1.4E-5
Oxygen diffusivity in nitrogen, $D_{\text{O}_2-\text{N}_2}$ ($\text{m}^2 \text{s}^{-1}$) [46,47]	1.8E-5
Carbon-dioxide diffusivity in water vapour, $D_{\text{CO}_2-\text{H}_2\text{O}}$ ($\text{m}^2 \text{s}^{-1}$) [46,47]	1.62E-5
Carbon-dioxide diffusivity in nitrogen, $D_{\text{CO}_2-\text{N}_2}$ ($\text{m}^2 \text{s}^{-1}$) [46,47]	1.6E-5
Hydrogen diffusivity in liquid electrolyte, $D_{\text{H}_2}^l$ ($\text{m}^2 \text{s}^{-1}$) [25]	1E-7
Oxygen diffusivity in liquid electrolyte, $D_{\text{O}_2}^l$ ($\text{m}^2 \text{s}^{-1}$) [25,29]	3E-7
Carbon-dioxide diffusivity in liquid electrolyte, $D_{\text{CO}_2}^l$ ($\text{m}^2 \text{s}^{-1}$) [25,29]	1E-7
Water vapour diffusivity in liquid electrolyte, $D_{\text{H}_2\text{O}}^l$ ($\text{m}^2 \text{s}^{-1}$)	1E-7
Nitrogen diffusivity in liquid electrolyte, $D_{\text{N}_2}^l$ ($\text{m}^2 \text{s}^{-1}$)	1E-7
Standard entropy change of anode, ΔS_a ($\text{J mol}^{-1} \text{K}^{-1}$) [45]	54.56
Standard entropy change of cathode, ΔS_c ($\text{J mol}^{-1} \text{K}^{-1}$) [45]	-216.2
Standard entropy change of generation reaction, ΔS_{tot} ($\text{J mol}^{-1} \text{K}^{-1}$) [45]	-161.64

order to add several capabilities (e.g. non-standard transport equations, source terms, temperature dependent properties, etc.) to ANSYS FLUENT 12.0.1. The SIMPLE algorithm is implemented for the coupling between the pressure and velocity field. An algebraic multi-grid (AMG) method with a Gauss–Seidel type smoother is used to accelerate the convergence. A strict convergence criterion with a residual of 10^{-10} is used for all variables.

3. Results and discussion

3.1. Model verification and validation

It is generally acknowledged that model validation is the most significant step in the model building sequence of numerical simulations. It is also one of the most overlooked. In this study, with the purpose of achieving highly accurate results, the experimental study by Brouwer et al. [48] and Lee et al. [49] are selected to investigate the model trustworthiness. In fact, the mathematical model is validated by means of the most popular criterion, the

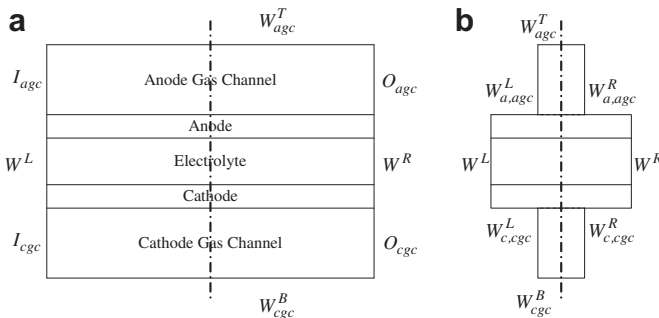


Fig. 3. Boundary conditions for the MCFC model: (a) front view, (b) side view.

polarization curve. In the first step, the model is built based on the reported geometry and operating conditions in [49]. In brief, the authors conducted several experiments to examine the performance of a single MCFC with a planar area of 100 cm^2 . The electrode–electrolyte assembly consisted of a 0.77 mm Ni–Cr alloy anode and a 0.72 mm in situ oxidized NiO cathode. A 62 mol % Li_2CO_3 , 38 mol % K_2CO_3 eutectic carbonate was utilized as electrolyte, and LiAlO_2 with Al_2O_3 fiber was fabricated as matrix material. At the anode side, a gaseous mixture of H_2 , H_2O and CO_2 with molar fractions of 0.69, 0.14 and 0.17 was used while in the cathode side, a mixture of O_2 , CO_2 and N_2 with molar fractions of 0.15, 0.30 and 0.55 was fed into the system. Base on these conditions the polarization curve at various operating condition was obtained [49].

In this study, the polarization curve at atmospheric pressure is initially used to verify and adjust the model input parameters. The two most common mechanisms for the cathode electrochemical reaction rate, namely the peroxide and superoxide mechanisms, are employed to investigate the validity of the model. Details of these mechanisms will be discussed in the following section. In the next step, the verified model is put in to practice to predict the polarization curve for another MCFC, reported in [48]. This step serves as the validation process. In conclusion, the verification and validation outcome is summarized in Figs. 4 and 5. The former illustrates the measured [49] and verified values based on the model fine-tuning. In contrast, the latter demonstrates the accuracy of the verified model in comparison with another experimental study [48] and also a numerical study. It can be easily observed that the model prediction have matched the experimental data adequately. Based on these two strict steps of verification and validation processes, the developed mathematical model is deemed functional in the sense that the model addresses the right problem and presents accurate results. Thereafter, the validated model is engaged in several simulation cases to examine polarization characteristics of a unit cell at relatively high utilization for cathode gas.

3.2. MCFC behaviour at high cathode gas utilization

In general, the first region of a fuel cell polarization curve, the so-called activation polarization region, occurs due to the sluggishness of the electrochemical reaction at low current densities (or

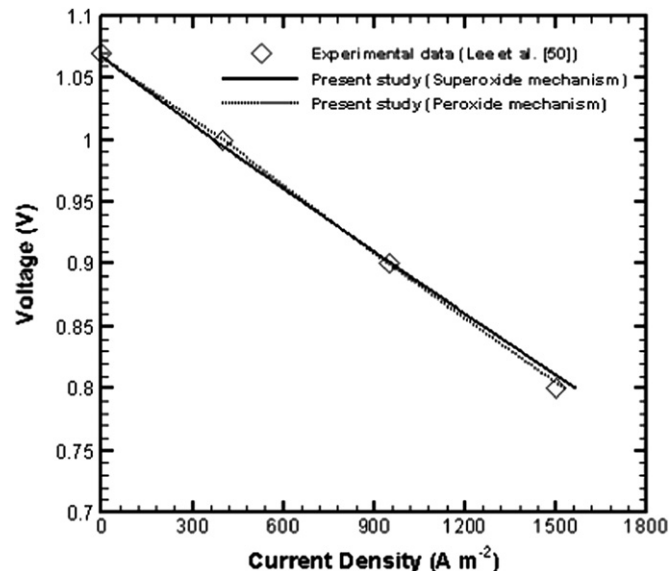


Fig. 4. Model parameter verification: based on peroxide and superoxide mechanism for cathode electrochemical reaction rate using the experimental study by Lee et al. [49].

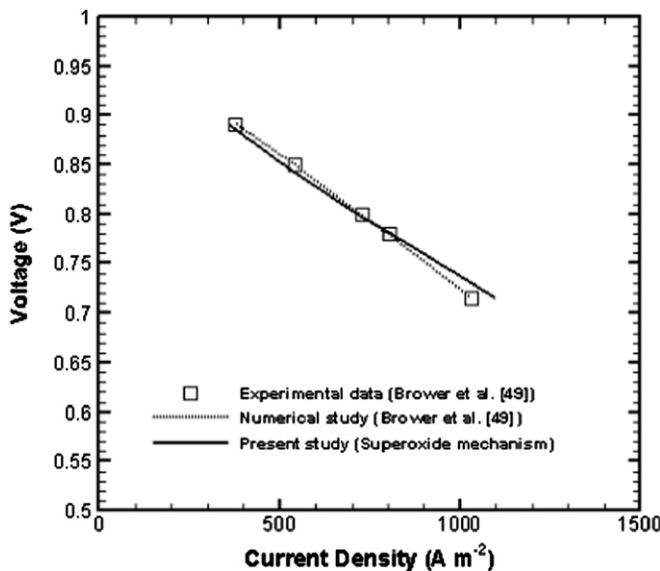


Fig. 5. Model validation: based on superoxide mechanism for cathode electrochemical reaction rate using the experimental and numerical study by Brouwer et al. [48].

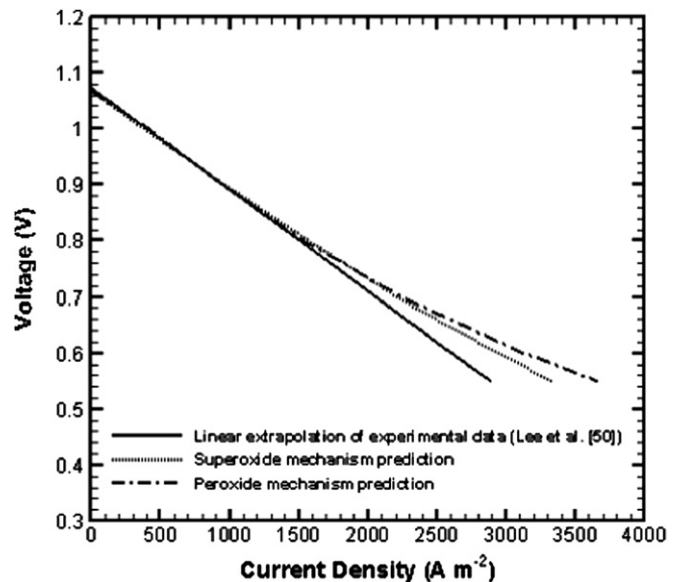


Fig. 6. Evaluation of polarization curve linearity between the model predictions (superoxide and peroxide mechanisms) and a linear extrapolation of experimental data [49].

voltage losses) across the cell. Boosting the supplied gas temperature provides some of the activation energy required to drive the electrochemical reaction. However, in molten carbonate fuel cells this region vanishes since the operating temperature is very high. This could be observed both in Figs. 4 and 5. Therefore, the polarization curve straight away starts with a linear behaviour which is due to the ohmic polarization. This is the practical and useful region of any fuel cell which is normally followed by a bent downwards. Conversely, opposite behaviour is observed in the simulated MCFC, shown in Fig. 6. In fact, Fig. 6 implies that using the prevailing reaction mechanisms, the linear behaviour could be achieved flawlessly but only for low and moderate current densities or cathode gas utilizations. It is worthwhile to mention that almost all previous experimental and numerical studies for MCFCs have only shown completely linear polarization curves. In Fig. 6, first the experimental data [49], which were used for the verification process, are extrapolated linearly in order to estimate the MCFC polarization characteristics at higher current densities. Then the model predictions, based on the two most common cathode mechanisms, are included. It is observed that model predictions demonstrate an upwards bent. This has been rarely discussed in the literature.

This paper reveals why the downwards curve is not reported in numerical studies. Noticeably, the issue was found to be in the porous cathode. In actual fact, it is expected that as the gaseous reactants are being consumed to produce current, the mass transfer process becomes dominant in controlling the fuel cell performance. In other words, the availability of gas mixture components turns out to be crucial which should lead to a drop off in the amount of current generation. Nevertheless, Figs. 7 and 8 show different trends. These graphs demonstrate the variation of local cathode volumetric current density (or carbonate ion generation rate) with carbon-dioxide utilization for various overpotentials using peroxide and superoxide mechanisms. Both mechanisms show an exponentially rising tendency (for all overpotential values) as the carbon-dioxide mole fraction is decreased. The peroxide mechanism (Fig. 7) indicates the fact that the volumetric generation of current is increasing up to a point where there is almost no carbon-dioxide left in the cathode. Higher overpotentials exacerbate the situation. The same growing trend may be observed from Fig. 8 for

the superoxide mechanism which is less utilized compared with the peroxide mechanism. However, for lower values of overpotentials, the rate of reaction decreases as the utilization reaches almost 80%. Therefore, because of the tendency in reaction rate (or volumetric current density) to increase with falling CO_2 , it is obvious that these mechanisms will never predict a downwards bent in the polarization curve. This could be justified by looking back at Eq. (21) which describes the cathode electrochemical reaction rate or volumetric current density. It suggests that the negative exponent of the oxygen mole fraction causes larger values at lower mole fractions. According to Table 2, the magnitude of this negative value is greater for the peroxide mechanism which creates a bigger divergence from the linear curve in Fig. 6.

In conclusion, the literature seems to lack experimental and numerical data for polarization curve at extremely high cathode gas utilizations (high average current densities). Investigations have

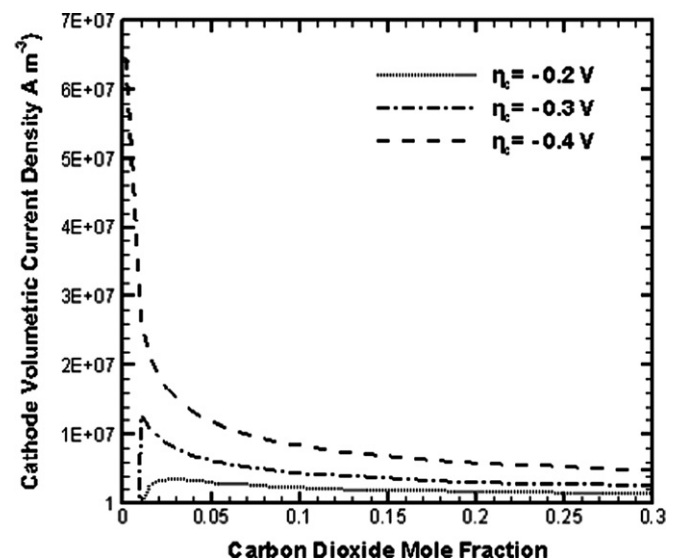


Fig. 7. Variation of cathode volumetric current density with carbon-dioxide utilization in various overpotentials using peroxide mechanism for cathode reaction rate.

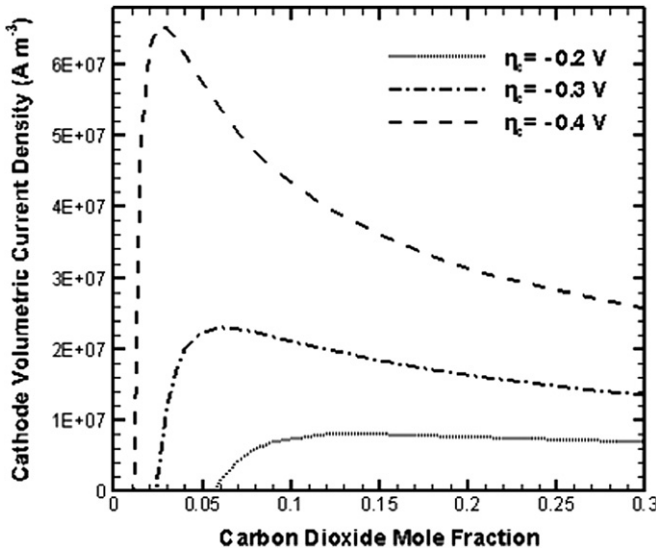


Fig. 8. Variation of cathode volumetric current density with carbon-dioxide utilization in various overpotentials using superoxide mechanism for cathode reaction rate.

always been conducted at low and moderate current densities, namely the practical operating region. This research shows that none of the available cathode reaction mechanisms can predict the MCFC behaviour at high cathode gas utilizations. This issue is related to the current correlations for cathode reaction rate [12,14] which characterize only apparent values without considering the true kinetics. Perhaps, one way to obtain a good fit to the experimental data at high current densities is to assign a positive exponent to CO₂ in Eq. (21). Changing this exponent at very low concentration could be another alternative. In any case, conducting further experimental analysis would be helpful to check whether the prediction in Fig. 9 is accurate. In contrast to the MCFCs, the downwards bent exists in the polarization curve of proton exchange membrane fuel cells (e.g., [50,51]) and solid oxide fuel cells ([52,53]). They both have positive exponents for reaction orders.

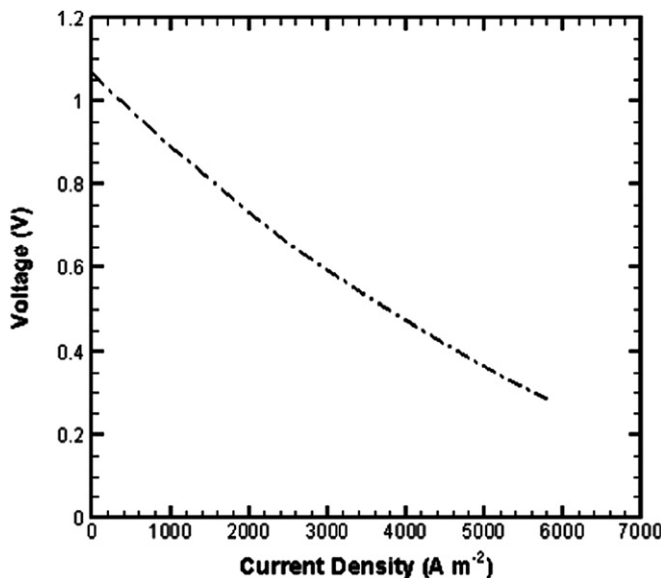


Fig. 9. Polarization curve obtained by using superoxide mechanism for cathode reaction rate.

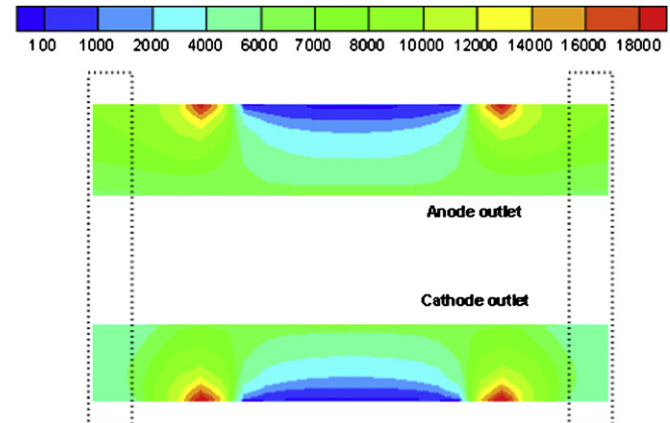


Fig. 10. Local current density (A m⁻²) distribution in anode and cathode outlet—anode mechanism: Ang and Sammels, cathode mechanism: Superoxide (operating voltage: 0.28 V).

Fig. 9 is obtained by conducting several simulations for different cell voltages. Each simulation results a point (voltage–current density) in this figure. By connecting these points the polarization curve is achieved. However, the code did not converge for the simulations in which the cell voltage was below 0.28 V.

In general, at the end of the simulation, once the electrolyte phase and solid phase potentials are determined in the anode, cathode and electrolyte, the local current density is calculated using Eqs. (42) and (43). Thereafter, the average current density of the electrode is determined by

$$\bar{J} = \frac{1}{A} \left(\int_A J_e dA \right) \quad (44)$$

where A is the electrode–electrolyte interface area, which should match for both anode and cathode. In the case that the simulation reaches convergence, the calculated average current density in anode and cathode are identical. As well, the local distribution of current density in anode and cathode are similar. In contrast, according to Fig. 10, non-uniformity in local volumetric current density started to occur after $V = 0.28$ V and different values for average current density were obtained (Fig. 11). Apparently, Fig. 10 shows that by lowering the cell voltage right after 0.28 V, which corresponds to 0.79 V drop in cell voltage, the local current density at the cathode corners (shown in dotted-box) diminishes. In other words, it declines by a factor of 2 comparing to the anode local current density at the same spot. This could be explained by taking

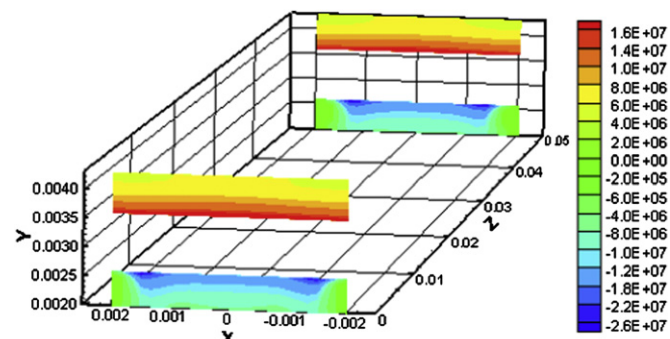


Fig. 11. Local volumetric current density (A m⁻³) distribution in anode and cathode inlet and outlet—anode mechanism: Ang and Sammels, cathode mechanism: Superoxide (operating voltage: 0.28 V).

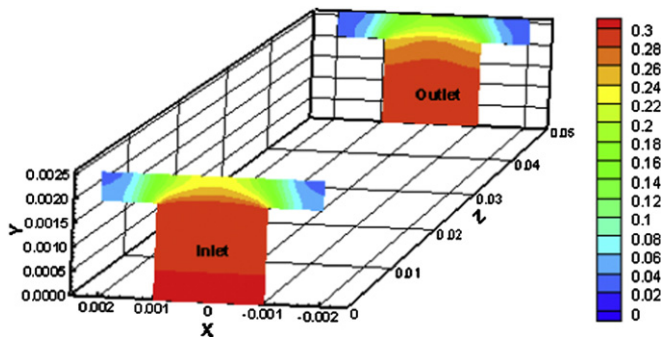


Fig. 12. Superoxide mechanism prediction for carbon-dioxide mole fraction at cathode and cathode gas channel (operating voltage: 0.28 V).

Fig. 11 into consideration. It simply demonstrates the sluggishness of the reaction rate or volumetric current density at the corners. In fact, in this extreme condition, the cathode electrochemical reaction occurs mainly under the gas channel and partially in a small spot close to the gas channel. Since the rate of reaction is decreased, the amount of generated current is reduced. Consequently, non-uniformity of the local current density deteriorates the MCFC performance. In realistic operating condition, the same current has to transfer through electrode–electrolyte assembly. However, the local current density is not necessarily uniform. The surface area through which the current is transferred, determines the current density and its area-weighted surface integral identifies the cell total current density. Our mathematical model perfectly predicts this equality hence this value was used to generate the polarization curves up to $V = 0.28$ V. At this voltage, the anode and cathode average current density calculated as 6343 and 5740 A m^{-2} which means they are not identical to any further extent. This is all due to the extremely small molar fraction of carbon-dioxide (and consequently oxygen) in the cathode corners shown in **Fig. 12**. This figure shows the local molar fraction of carbon-dioxide in cathode and cathode gas channel inlet and outlet. It is obvious that carbon-dioxide utilization reaches its highest value at the cathode corners and the electrochemical reaction rate finds smaller values at these spots. Therefore, the lack of reactants in high current densities (or high utilizations) is the source of all non-uniformity and performance deterioration.

4. Conclusions

A detailed three-dimensional, mathematical model of an MCFC was presented by employing volume-averaged equations. Two different mechanisms were incorporated for the cathode electrochemical reaction rate. ANSYS FLUENT 12.0.1, a finite volume based commercial software package, was utilized to solve the system of partial differential equations. The following concluding remarks are drawn from this study:

- For a specific case, available experimental data were used to adjust model input parameter.
- The verified model was employed to check the validity of the results by conducting a comparison with another experimental study and good agreement was achieved.
- Both peroxide and superoxide mechanisms predicted the linear region of the polarization curve accurately. This occurs for low and moderate voltage losses, or low to moderate cathode gas utilizations.
- Both mechanisms showed a concave tendency for the cathode reaction rate as the carbon-dioxide mole fraction is decreased when the current density increases.

- None of these mechanisms showed a downward bent in the polarization curve.
- The negative exponent of the oxygen mole fraction was identified to be the causes of larger reaction rates at lower O_2 mole fractions.
- Larger negative exponent for the cathode reaction rate of the peroxide mechanism (as compared to the superoxide mechanism) created a larger divergence from the linearity in the polarization curve.
- Using positive exponents for the oxygen in the cathode reaction rate would probably result in obtaining a good fit to the experimental data at high current densities.
- At extreme conditions (high voltage losses), the local current density at the cathode corners declines by a factor of 2.
- At high voltage drops, the cathode electrochemical reaction occurs mainly under the gas channel and partially in a small location close to the gas channel.
- The lack of reactants at high current densities (or high utilizations) is the source of all non-uniformity and performance deterioration.

Acknowledgements

The support for this research by the Ontario Research Fund and the Natural Sciences and Engineering Research Council of Canada is gratefully acknowledged.

References

- [1] M. Bischoff, Journal of Power Sources 154 (2006) 461–466.
- [2] I. Zabalza, A. Aranda, M.D. de Gracia, International Journal of Hydrogen Energy 32 (2007) 1396–1403.
- [3] L.G. Austin, M. Ariet, R.D. Walker, G.B. Wood, R.H. Comyn, Industrial & Engineering Chemistry Fundamentals 4 (1965) 321–326.
- [4] F.G. Will, D.J.B. Daniel, Journal of Electrochemical Society 119 (1969) 933–937.
- [5] S. Srinivas, H.D. Hurwitz, Electrochimica Acta 12 (1967) 495–500.
- [6] L.F. Albright, J.T. Cobb Jr., Electrochemical Society Journal 115 (1968) 2–6.
- [7] R.P. Iczkowski, Journal of the Electrochemical Society 111 (1964) 1078–1086.
- [8] R.C. Burshtein, V.X. Markin, A.G. Psheniohnikov, V.A. Chismadzev, Y.G. Chirkov, Electrochimica Acta 9 (1964) 773–787.
- [9] E.A. Grens, Industrial and Engineering Chemistry Fundamentals 5 (1966) 542–547.
- [10] R. Brown, L.A. Horve, Journal of the Electrochemical Society 113 (1966) C197–C201.
- [11] J. Giner, C. Hunter, Journal of the Electrochemical Society 116 (1969) 1124–1128.
- [12] C.Y. Yuh, J.R. Selman, Journal of Electrochemical Society 131 (1984) 2062–2069.
- [13] G. Wilenski, Journal of the Electrochemical Society 130 (1983) 117–121.
- [14] H.R. Kunz, L.J. Bergoli, T. Szymanski, Journal of Electrochemical Society 131 (1984) 2815–2821.
- [15] J. Jewulski, L. Suski, Journal of Applied Electrochemistry 14 (1984) 135–143.
- [16] J. Jewulski, Journal of Applied Electrochemistry 16 (1986) 643–653.
- [17] G.L. Lee, J.R. Selman, L. Plomp, Journal of the Electrochemical Society 140 (1993) 390–396.
- [18] E. Fontes, C. Lagergren, D. Simonsson, Electrochimica Acta 38 (1993) 2669–2682.
- [19] J.A. Prins-Jansen, K. Hemmes, H.W. De Wit, Electrochimica Acta 42 (1997) 3585–3600.
- [20] E. Fontes, M. Fontes, D. Simonsson, Electrochimica Acta 41 (1996) 1–13.
- [21] E. Fontes, C. Lagergren, G. Lindbergh, D. Simonsson, Journal of Applied Electrochemistry 27 (1997) 1149–1156.
- [22] J.D. Fehribach, J.A. Prins-Jansen, K. Hemmes, J.H.W. De Wit, F.W. Call, Journal of Applied Electrochemistry 30 (2000) 1015–1021.
- [23] J.D. Fehribach, K. Hemmes, Journal of Electrochemical Society 148 (2001) A783–A787.
- [24] J.D. Fehribach, European Journal of Applied Mathematics 12 (2001) 77–96.
- [25] N. Subramanian, B.S. Haran, P. Ganeshan, R.E. White, B.N. Popov, Journal of the Electrochemical Society 150 (2003) A46–A56.
- [26] N. Subramanian, B.S. Haran, R.E. White, B.N. Popov, Journal of the Electrochemical Society 150 (2003) A1360–A1367.
- [27] J.A. Prins-Jansen, J.D. Fehribach, K. Hemmes, H.W. de Wit, Journal of Electrochemical Society 143 (5) (1996) 1617–1628.
- [28] ANSYS FLUENT 12.0.1 User's Guide, Ansys Inc, 2009.
- [29] R.B. Bird, W.E. Stewart, E.N. Lightfoot, Transport Phenomena, John Wiley & Sons, New York, 1960.

[30] Q. Ye, T.V. Nguyen, *Journal of the Electrochemical Society* 154 (2007) B1242–B1251.

[31] A. Boden, G. Lindbergh, *Journal of the Electrochemical Society* 153 (2006) A2111–A2119.

[32] J.E. Findlay, Mass transport in the cathode electrode of a molten carbonate fuel cell, Masters thesis, University of Ontario Institute of Technology, 2009.

[33] D.A. Nield, A. Bejan, in: *Convection in Porous Media*, second ed.. Springer, New York, 1999.

[34] L.J. Yu, G.P. Ren, X.M. Jiang, J.Q. Yuan, G.Y. Cao, *Brazilian Journal of Chemical Engineering* 24 (04) (2007) 523–533.

[35] J. Kui, Experimental and modelling studies of cold start processes in proton exchange membrane fuel cells, Ph.D. thesis, University of Waterloo, 2011.

[36] K. Promislow, P. Chang, H. Haas, B. Wetton, *Journal of the Electrochemical Society* 155 (7) (2008) A494–A504.

[37] J. Bear, Y. Bachmat, *Introduction to Modeling of Transport Phenomena in Porous Media*, Kluwer, Dordrecht, The Netherlands, 1991.

[38] P.G.P. Ang, A.F. Sammells, *Journal of Electrochemical Society* 127 (1980) 1287–1294.

[39] M.Y. Ramandi, I. Dincer, *Journal of Power Sources* 196 (2011) 8509–8518.

[40] V. Verda, A. Sciacovelli, *Applied Thermal Engineering* 31 (2011) 2740–2748.

[41] C.Y. Wang, *Chemical Reviews* 104 (12) (2004) 4727–4766.

[42] Z. Ma, S.M. Jeter, A.I. Abdel-Khalik, *International Journal of Hydrogen Energy* 28 (2003) 85–97.

[43] J. Wee, K. Lee, *International Journal of Energy Research* 30 (2006) 599–618.

[44] Y.S. Xu, Y. Liu, X.Z. Xu, G.X. Huang, *Journal of the Electrochemical Society* 153 (2006) A607–A613.

[45] F. Yoshiba, *International Journal of Energy Research* 28 (2004) 1361–1377.

[46] W.M. Haynes (Ed.), *CRC Handbook of Chemistry and Physics*, first ed. CRC Press/Taylor and Francis, 2011. Internet Version.

[47] X. Li, *Principles of Fuel Cells*, Taylor & Francis, New York, 2005.

[48] J. Brouwer, F. Jabbari, E. Martins Leal, T. Orr, *Journal of Power Sources* 158 (2006) 213–224.

[49] C. Lee, D. Kim, H. Lim, *Journal of Electrochemical Society* 154 (2007) B396–B404.

[50] J. Shi, X. Xue, *Chemical Engineering Journal* 163 (2010) 119–125.

[51] J. Shi, X. Xue, *Electrochemical Acta* 55 (2010) 5263–5273.

[52] A. Kazim, H.T. Liu, P. Forges, *Journal of Applied Electrochemistry* 29 (1999) 1409–1416.

[53] H. Wu, P. Berg, X. Li, *Journal of Electrochemical Society* 157 (2010) B1–B12.